Dovepress
Taylor & Francis Group

ORIGINAL RESEARCH

Self-Assembled Nanoplatform with pH/NIR Light-Responsive Drug Delivery for Combined Therapy of Glioma in vitro

Zhiping Cao[1,2], Haiyan Gao[2], Yong Xu 🔟[1]

[1]Department of Clinical Psychology, The Eighth Affiliated Hospital, Sun Yat-Sen University, Shenzhen, People's Republic of China; [2]School of Biomedical Sciences, Faculty of Medicine, The Chinese University of Hong Kong, Hong Kong, People's Republic of China

Correspondence: Haiyan Gao; Yong Xu, Email haiyangao@cuhk.edu.hk; xuyongsmu@vip.163.com

Purpose: The integration of multifunctional components into a single nanoplatform offers significant potential for personalized and minimally invasive therapeutic applications. Herein, we present a facile yet versatile strategy to engineer a near-infrared (NIR) pH- and light-responsive nanomaterial, demonstrating promising efficacy in glioblastoma combination therapy through multimodal synergistic mechanisms.

Methods: The FEID nanoplatform was engineered by co-assembling ICG, DOX, and Fe^{3+}. Systematic characterization included physicochemical properties (TEM, DLS, UV-vis-NIR spectroscopy, zeta potential measurements, and XPS), photothermal conversion efficiency, Fenton reaction kinetics, PTT-enhanced CDT performance, laser-triggered drug release patterns, and NIR-responsive drug release and dual-modal imaging (fluorescence/MRI) capabilities. Intracellular DOX accumulation and ROS generation were confirmed by confocal laser scanning microscopy and flow cytometry in U87 glioma cells. Hemolysis assay, cytotoxicity profiling against normal 293T and RAW264.7 cells, and H&E staining were applied for biosafety assessment. The synergistic anti-glioblastoma efficacy was systematically evaluated through MTT assays, live/dead cell staining, and apoptosis detection via Annexin V/PI staining. The pharmacokinetic profiles and blood-brain barrier (BBB) permeability of the FEID were analyzed in vivo.

Results: The FEID nanoplatform displayed uniform spherical morphology (78.2 nm average diameter). pH/NIR-triggered release of DOX (chemotherapy) and ICG (PTT), combined with GSH depletion and NIR irradiation, synergistically enhanced Fe^{2+}-mediated CDT. This multimodal therapy demonstrated potent cytotoxicity against U87 glioblastoma cells (14.8% cell viability). Furthermore, ICG fluorescence recovery and MRI contrast enabled tumor imaging, while enhanced BBB permeability ensured effective drug delivery for in situ glioma treatment.

Conclusion: In summary, we developed a safe FEID anti-tumor nanoplatform through a simple self-assembly process. This platform demonstrates the potential for controlled drug release and efficient combination therapy.

Keywords: intelligent drug delivery system, responsive drug release, fluorescence recovery, combination therapy

Introduction

Glioblastoma (GBM) represents one of the most common primary intracranial tumors.[1] The combination of radiotherapy and the chemotherapeutic drug temozolomide has been established as the standard first-line treatment for GBM.[2] However, therapeutic resistance to both radiotherapy and chemotherapy remains a major clinical challenge in glioblastoma (GBM), frequently leading to tumor recurrence and poor patient survival.[3] This resistance primarily stems from tumor heterogeneity and the immunosuppressive tumor microenvironment (TME). A promising therapeutic strategy involves exploiting the inherent oxidative stress vulnerability of tumor cells by precisely inducing a reactive oxygen species (ROS) storm, which could simultaneously overcome immunosuppression while achieving direct tumor eradication.

Reactive oxygen species (ROS), including superoxide anion, hydrogen peroxide (H_2O_2), singlet oxygen, and hydroxyl radical (•OH), play a crucial role in the process of cancer treatment as they effectively eliminate cancer cells by

damaging essential biological macromolecules, such as lipids, proteins, and DNA.[4–6] The integration of nanomaterials in medicine has led to the discovery of diverse unique nanomaterials that effectively modulate ROS levels and regulate their dynamic behavior in biological system.[7–10] Moreover, various anticancer strategies have been developed to stimulate ROS production, including photodynamic therapy (PDT), sonodynamic therapy (SDT), radiotherapy (RT), and chemo-dynamic therapy (CDT).[11–14] As a novel cancer treatment strategy, CDT utilizes Fenton or Fenton-like reaction to specifically generate •OH in the tumor area.[15] However, the efficiency of CDT is severely compromised by insufficient H_2O_2 concentrations and elevated glutathione (GSH) levels in the tumor microenvironment. Additionally, many CDT reagents demonstrate poor catalytic performance and degradability. Therefore, enhancing CDT efficiency remains a critical priority.

Multimodal collaborative treatment is garnering significant attention due to its potential to enhance treatment outcomes through the synergistic integration of diverse treatment approaches. Compared to single-modality treatments, multimodal therapy can incorporate the advantages of different treatments into a single nanosystem, achieving synergistic treatment effects (illustratively stated as "1+1>2"). Recent years have witnessed a substantial increase in CDT-based combination cancer therapies, including CDT-PTT, CDT-PDT, CDT-chemotherapy, CDT-SDT, CDT-RT, CDT-immunotherapy, and various other effective combined therapies.[16–19] As a common external excitation energy source, PTT utilizes near-infrared light to irradiate photothermal agents (PTAs), generating heat that effectively induces tumor cell necrosis or apoptosis.[20,21] When combined with CDT, PTT demonstrates remarkable synergistic effects. Specifically, the PPT-induced temperature elevation enhances the catalytic efficiency of the Fenton/Fenton-like reaction, thereby augmenting its efficacy.[22] Moreover, local hyperthermia effectively eliminates tumor cells while concurrently stimulating blood circulation, improving oxygenation within the hypoxic tumor regions, and ultimately fostering a more favorable microenvironment for CDT.[23] Furthermore, chemotherapeutic agents can enhance CDT effects by increasing H_2O_2 concentration.[24,25] Therefore, the combination of CDT with PTT and chemotherapy presents a promising and versatile therapeutic strategy.

Stimuli-responsive nanomaterials have garnered significant research attention owing to their potential for precision therapy. These intelligent nanoplatforms, engineered to respond to tumor microenvironment (TME) characteristics, substantially enhance anticancer therapeutic efficacy through multiple mechanisms: (1) improved tumor targeting, (2) spatiotemporally controlled drug release, and (3) integrated theranostic capabilities. Such multimodal functionality not only increases treatment precision but also minimizes systemic toxicity. For instance, the acidic tumor microenvironment can trigger pH-responsive material degradation or drug release.[26] Overexpressed enzymes (eg, matrix metalloproteinases/MMPs) may cleave therapeutic agents into smaller molecules, thereby enhancing their penetration through the dense tumor stroma.[27] Additionally, the elevated glutathione (GSH) levels characteristic of the tumor redox environment can cleave disulfide bonds to achieve controlled drug release.[28] Although endogenous stimulus-responsive materials have been extensively explored for cancer therapy, their clinical translation has been limited by insufficient response rates and suboptimal drug release kinetics. To address these limitations, researchers have incorporated external stimuli-responsive mechanisms to enhance therapeutic precision. Over the past decade, various smart drug carriers responsive to extra-cellular stimuli have been developed for cancer treatment, including: (1) polyamidoamine dendrimers (UV light-responsive),[29] (2) polymer nanoparticles and upconversion nanoparticles (NIR light-responsive),[30] (3) superparamagnetic nanoparticles (magnetically responsive),[31] and (4) microbubbles (ultrasound-responsive).[32] The development of dual-responsive nanoplatforms that integrate both endogenous and external stimuli shows particular promise for achieving spatiotemporally controlled drug release with enhanced therapeutic efficacy.

Advances in imaging technology hold transformative significance for tumor diagnosis and therapy. While MRI remains a paramount preoperative diagnostic method for GBM,[33] it has inherent limitations, including suboptimal resolution and reduced sensitivity. Near-infrared fluorescence (NIRF) imaging technology serves as a good complement to MRI, providing sensitive imaging with high temporal resolution, enabling selective visualization of pathological organs through fluorescent probes targeting specific biological tissues.[34,35] For example, indocyanine green (ICG) and methylene blue, play critical roles in near-infrared fluorescence imaging of tumors.[36,37] However, the poor photostability and concentration dependent quenching of ICG limit its application. Moreover, conventional "always-on" fluorescent probes, which emit continuous fluorescent signals, result in poor signal-to-noise ratios for targeted visualization. To address this limitation, stimulus
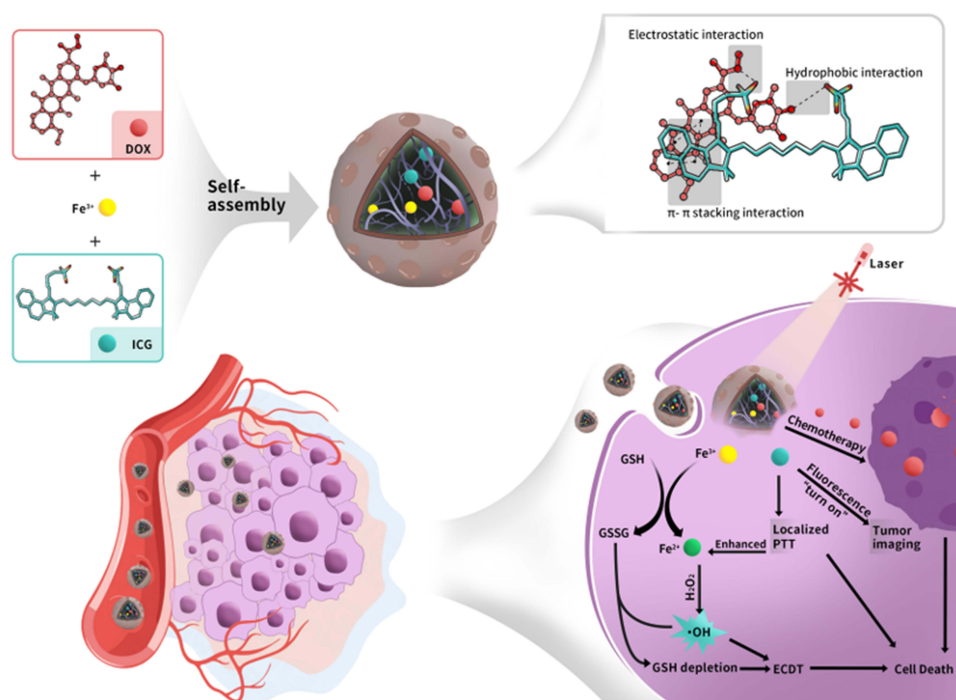
Scheme 1 The scheme of FEID nanoparticle synthesis and its biomedical applications. Preparation procedure for FEID and pH/near infrared light-triggered imaging-guided combined CDT/PTT/chemotherapy.

responsive fluorescence imaging technology has been developed to achieve controlled activation of nanomaterials and generation of fluorescent signals. This approach significantly enhances tumor diagnostic accuracy, minimizes side effects, and potentially facilitates precise tumor treatment.[38–40] Therefore, the integration of MRI with responsive near-infrared fluorescence imaging could substantially improve both the specificity and sensitivity of tumor imaging.

In this study, we developed a novel multimodal imaging and therapeutic platform, Fe-ICG-DOX (FEID) nanomedicine, with dual responsiveness to pH and near-infrared light by incorporating ICG, doxorubicin (DOX), and ferric chloride ($FeCl_3$). ICG is a clinically approved NIR dye with both photothermal and photodynamic activities, DOX is a common chemotherapy drug for cancer treatment. This carrier free drug delivery system responds to both pH and near-infrared light, effectively delivering therapeutic drugs to the tumor site, preventing premature drug leakage and potential carrier related toxicity. The FEID rapidly disassembles under acidic conditions and local hyperthermia at tumor sites, followed by Fe^{3+}/Fe^{2+}-catalyzed decomposition of H_2O_2, generating highly toxic •OH through Fenton-like reactions for CDT. Concurrently, the released DOX facilitates cancer chemotherapy. Furthermore, ICG-induced hyperthermia accelerates the Fenton-like reaction, DOX release and enables tumor PTT. Fe^{3+}-mediated GSH deprivation additionally enhances Fenton reaction efficiency. Notably, FEID exhibits recovered fluorescent signals at tumor sites, generating high-contrast imaging that enables fluorescence/magnetic resonance dual-modality imaging to guide CDT/PTT/chemotherapy combination therapy (Scheme 1). The FEID system demonstrates multiple advantages, including simple synthesis procedures, straightforward composition and structure, targeted drug release, and controllable fluorescence signals. These findings establish a promising platform for enhancing the precision and efficacy of cancer therapy.

Materials and Methods
Materials
DOX, ICG, and $FeCl_3$ were obtained from Dalian Meilun Biotech Co., Ltd (Dalian, China). Calcein-AM and propidium iodide (PI) were obtained from Solarbio Technology Co., Ltd (Beijing, China). 1,10-Phenanthroline monohydrate (Phe), methylene blue (MB), and 3,3′,5,5′-Tetramethylbenzidine (TMB) were purchased from Macklin Biochemical Co., Ltd (Shanghai, China). 2′,7′-Dichlorodihydrofluorescein diacetate (DCFH-DA) was purchased from Beyotime

9057

Biotechnology. 3-(4,5-dimethyl-2-thiazolyl)-2,5-diphenyl-2-H-tetrazolium bromide (MTT) was obtained from Sigma Chemical Corporation (USA). Annexin V-APC Apoptosis Detection Kit (PI) was purchased from Simu Biotechnology Co., Ltd (Tianjin, China). All other chemicals were of reagent grade. Water was purified with a Milli-Q Plus 185 water purification system (Millipore, Bedford, MA).

Cell Culture and Animals

293T cells (STCC10301P), RAW 264.7 cells (STCC20020P), and U87MG cells (STCC00014P) were all obtained from Wuhan Service Biotechnology Co., Ltd. The above cells were cultured in complete Dulbecco's Modified Eagle Medium (DMEM) supplemented with 10% fetal bovine serum (FBS) and 1% antibiotics (penicillin and streptomycin) at 37°C with 5% CO_2.

Adult c57BL/6 male mice (25–45g) were used in this study. Animals were bred and maintained by the Laboratory Animal Service Centre of The Chinese University of Hong Kong (CUHK). All animal procedures were approved by the Animal Experimentations and Ethics Committee (AEEC number: 18–232-MIS-5-C) at the Chinese University of Hong Kong (Animal license number: (21–340) in DH/HT&A/8/2/1 Pt.18), which strives to uphold the highest international standards in animal care and welfare, and conducts teaching and research involving live animals in accordance with Cap 340 Animals (Control of Experiments) Ordinance, The Hong Kong Code of Practice for Care and Use of Animals for Experimental Purposes.

Preparation and Characterization of the FEID

We employed two distinct methods for the fabrication of FEID. In the initial approach, an aqueous solution comprising ferric chloride, indocyanine green, and doxorubicin were combined at a 1:1:1 mass ratio. The mixture was then vigorously shaken for 12 hours at 28°C and 300 rpm in a light-free environment. Alternatively, in the second method, ferric chloride and indocyanine green aqueous solutions were initially mixed at a 1:1 mass ratio for 3 h. Subsequently, the doxorubicin aqueous solution was added, and the resulting mixture further oscillated at a 1:1:1 mass ratio for 9 hours under conditions of 300 rpm and 28°C, while being shielded from light. Following preparation, the FEID were collected and subjected to three washes through repeated centrifugation utilizing a 10 KD ultracentrifuge tube to eliminate any unbound molecules. The ultracentrifuge was operated at 4000 rpm and 37°C for a duration of 20 minutes. Next, the purified sterile diagnostic and therapeutic agent were obtained by filtration through a membrane filter and subsequently stored in a light-protected environment.

The morphology and structure of FEID were characterized using transmission electron microscopy (TEM, JEOL, Japan). The size and size distribution analysis were performed with the SZ-100 Nanoparticle Analyzer (Horiba Scientific). Ultraviolet-visible-near-infrared (UV-vis-NIR) absorption spectra were obtained using a microplate reader (Biotek Synergy H1, USA). X-ray photoelectron spectroscopy (XPS) was conducted with X-ray photoelectron spectroscopy (Thermo Scientific K-Alpha, USA). Iron content analysis was carried out using an inductive coupled plasma mass spectrometer (ICP-MS, Agilent 7800, USA).

Evaluation of Photothermal Effect

We investigated the photothermal effect of FEID due to the strong absorption in the NIR. FEID solutions with different concentrations (ICG concentration: 0 μg/mL, 100 μg/mL, 50 μg/mL, 25 μg/mL, 12.5 μg/mL, 6.25 μg/mL) and different solutions with the same ICG concentration (12.5 μg/mL) were continuously irradiated with an 808 nm laser at a power density of 1.0 W/cm^2 for 5 min. The temperature and thermal images of the solution were recorded using a FLIR A5 camera (USA) and quantified with BM IR software.

Evaluation of •OH Generation Ability of FEID and PTT-Enhanced Fenton-Like Reaction

The degradation of MB was assessed after capturing •OH, which served as an indicator for evaluating the quantity of •OH generated by the FEID Fenton reaction. Essentially, the Fenton reaction is a process in which Fe^{2+} catalyzes the highly expressed H_2O_2 in the TME to generate highly oxidized •OH (typical reaction scheme: $Fe^{2+} + H_2O_2 \rightarrow Fe^{3+} + OH• + OH^-$; $Fe^{3+} + H_2O_2 \rightarrow Fe^{2+} + HO_2• + H^+$). Briefly, the FEID ([Fe]=0.9mM) were introduced into a solution containing

MB (20 µg/mL) and H_2O_2 (100 µM). The mixture was allowed to stand for 20 min, and subsequently, the absorbance of the solution at 664 nm was measured using UV/VIS spectroscopy. A control group consisting of pure MB was utilized for comparison.

To investigate the ability of FEID to generate •OH under different pH conditions, the absorbance of the solution was recorded at various pH values (pH 3.2, 5.4, and 7.4). Furthermore, the enhanced Fenton-like performance through PTT was evaluated. The aforementioned mixture was subjected to irradiation with an 808 nm laser at pH 5.4 for 5 min, and the absorbance of the solution at 664 nm was observed.

Moreover, the production of •OH was also studied by monitoring changes in absorption using TMB as an indicator. Pure TMB and $FeCl_3$ were employed as control groups. FEID was added to a solution containing 0.2 mM TMB and 100 µM H_2O_2 at a pH of 5.4. With and without laser irradiation, the oxidation of TMB induced by •OH was monitored by measuring changes in absorbance intensity at 652 nm.

GSH-Depletion Ability of the FEID

To investigate the GSH depletion capacity of Fe^{3+} in FEID, we monitored the solution containing 0.2 mM Phe and FEID ([Fe]=0.9 mM) by measuring the change in absorbance intensity at 525 nm using a UV-Vis spectrophotometer, both in the presence and absence of GSH (10 mM). Additionally, we examined the absorbance intensity changes of FEID at 525 nm under acidic conditions (pH 7.4, 6.8, 5.4, and pH 5.4 + Laser) in the presence of GSH (10 mM) to evaluate their GSH depletion ability.

Fluorescence Imaging and Magnetic Resonance Imaging

Free ICG, Free DOX, Fe^{3+}-ICG, ICG-DOX, and FEID with various ICG concen- trations (100, 50, 25, 12.5 and 6.25 µg/ mL) were added to 96-well plate (200 µL) immersed at the same depth in ddH_2O with or without irradiation (1.0 W/cm^2, 5 min). Fluorescence images were acquired using the Carestream FX PRO fluorescence imaging system. Additionally, the MRI effect of FEID was examined using a clinical MRI scanner (3.0T) (United Imaging, China).

Evaluation of the DOX Release Ability of FEID

To assess the DOX loading and release, the concentration and absorbance data obtained from the standard curve at 480 nm can be utilized. For the in vitro release evaluation of DOX, a solution of 2 mL was introduced into a dialysis bag with a molecular weight cutoff (MWCO) of 10,000 Da. The dialysis bag was then placed inside a 50 mL centrifuge tube containing PBS at pH 5.4 and 7.4. The system was horizontally shaken at 37°C and 300 rpm. Subsequently, at the specific time point, 200 µL of the released solution was extracted and replaced with an equal volume of fresh PBS. The absorbance of the released DOX was measured at 480 nm. This procedure was repeated three times to ensure accuracy. To investigate the enhancement of DOX release through photothermal stimulation, the FEID solution was immersed in a PBS buffer at pH 5.4, and NIR irradiation was applied for 30 min. At designated time points, 100 µL of the dispersion was collected, and the absorbance of supernatant at 480 nm was measured using an ultraviolet-visible spectrophotometer to determine the DOX content. The encapsulation efficiency (EE) and loading efficiency (LE) of DOX or ICG are calculated as follows:

EE (%) = (weight of loaded drug) / (weight of initially added drug) × 100%;

LE (%) = (weight of loaded drug) / (total weight of NPs) × 100%.

The Biosafety of FEID

293T cells and RAW264.7 cells were seeded into 96-well plates containing 100 µL of medium and incubated overnight at 37°C under 5% CO_2, to obtain a density of 1×10^4 cells per well. Then, MTT assays were used to detect cellular viability of 293T cells and RAW264.7 cells. First, FEID at different concentrations of DOX (0, 2.5, 5, 7.5, 10 and 15 µg/mL) was added. After treatment for 24 h, the cells were washed with DMEM, 10 µL of 0.5 mg/mL MTT solution was added to each well, and then the cells were incubated at 37 °C for another 4 hours. The medium was then removed and dimethyl sulfoxide (DMSO, 150 µL) was added. Absorbance values were recorded at 570 nm using a microplate reader. The cell viability was calculated as follows: Viability (%) = (N1-N0) / (N2-N0) × 100% (N1 is the absorbance value of drug-

treated cells, N2 is the absorbance value of non-drug-treated cells, and N0 is the absorbance value of the blank group with neither cells nor drug treatment and only medium).

In Vitro Cellular Uptake

In order to study the uptake behavior of U87MG cells, U87MG cells were placed on a 6-well plate at a density of 1×10^5 cells per well. Subsequently, the cells were treated with pure DOX and FEID (DOX concentration: 2 μg/mL). Following a 12 h of incubation period, the wells incubated with FEID were then irradiated with $1 W/cm^2$ laser for 5 min and continued to be incubated in the cell incubator for 4 h. After that, the culture medium was removed, and the cells were washed thrice with PBS and fixed with 4% paraformaldehyde. Finally, nuclei were stained with DAPI for 10 min, washed with PBS three times again, and then visualized by confocal laser scanning microscope (CLSM, Nikon C2). Meanwhile, the U87MG cells were also visualized using an inverted fluorescence microscope (Olympus, IX73).

Since DOX has an excitation wavelength of 475–485 nm and an emission wavelength of 575–585 nm, cellular uptake study was also performed by flow cytometry (Luminex, Guava® easyCyteTM). U87MG cells were inoculated into 6-well plates at 5×10^5/well and incubated overnight at 37°C with 5% CO_2 to allow the cells to adhere to the wall. The cells were then treated with DOX, FEID ($C_{[DOX]}$ = 2 μg/mL) for another 12 h of incubation. One of the wells incubated with FEID was irradiated with a $1 W/cm^2$ laser for 5 min and incubated for another 4 h. Then the cells were washed three times with PBS, digested with trypsin, and centrifuged at 1000 rpm for 5 min, followed by washing twice with ice-cold PBS for analysis by using the flow cytometer (Luminex, Guava® easyCyteTM). The instrument is equipped with a 488 nm laser and a band-pass filter (525/30). The instrument was adjusted with untreated cells. The average fluorescence intensity of the cells was calculated using a histogram.

Evaluation of Intracellular ROS Production

U87MG cells were seeded in 6-well plates at a density of 5×10^5 cells per well. Following an overnight incubation in the CO_2 incubator at 37°C with 5% CO_2, the cells subjected to various treatment groups (DMEM, ICG, DOX, Fe^{3+}-ICG, ICG-DOX and FEID, the concentrations of DOX and ICG were 2 μg/mL and 12.5 μg/mL respectively) were studied and incubated in the dark for an additional 24 h. Subsequently, the cells were thoroughly washed three times with PBS. Next, cells in one of the wells, treated with FEID, were exposed to irradiation using an 808 nm laser, at a power density of 1 W/cm^2 for a duration of 5 min and incubated for another 4 h. The other FEID group was not irradiated as a control. Following this, the cells were once again washed three times with PBS before the addition of DCFH-DA (10 μM/mL) to the dish, allowing for a 30 min incubation. The medium was then removed, and the cells were meticulously washed and subsequently examined under an inverted fluorescence microscope for observation and analysis.

Evaluation of the Synergistic Therapeutic Effect in Vitro

First, MTT assay was performed in a 96-well cell plate to assess the efficacy of the combination therapy in vitro. U87MG cells were seeded into the wells at a density of 1×10^4 cells per well and cultured for 24 h to allow adherence at 37 °C with 5% CO_2. Following this, the medium was aspirated, and the cells were treated with serum medium containing various therapeutic agents for 24 h in a dark environment. Subsequently, the cells were washed with fresh culture medium and exposed to 1 W/cm^2 of 808 nm laser light for 5 min, followed by further incubation at 37 °C with 5% CO_2 for an additional 6 h. After washing the cells with PBS, they were incubated with MTT solution for 4 hours, the absorbance at 570 nm was measured using a plate reader.

To enhance the intuitive evaluation of cell survival following treatment with different groups, a 24-hour treatment period was employed, after which fresh DMEM replaced the culture medium to eliminate residual drugs. Cells were subjected to either 808 nm laser irradiation (1 W/cm^2, 5 min) or received no laser irradiation. After that, all cell groups were further cultured for an additional 6 h, stained with calcein AM and PI, and subsequently examined under a fluorescence microscope.

In addition, the synergistic anticancer efficacy of FEID NPs was investigated using Annexin-V/PI double staining. U87MG cells were seeded at a density of 1×10^5 per well in 12-well plates and cultured overnight. Different solutions (equivalent ICG concentration of 12.5 μg/mL) were added to the cells and incubated for 12 h, the supernatant was

discarded and fresh DMEM was added, and the cells treated with FEID were then irradiated with l808 nm laser (1 W/cm^2 for 5 min). All cell groups were further cultured for an additional 4 hours. Then the cells were harvested by trypsin digestion, washed with PBS, resuspended by adding 200 μL of Annexin V-APC conjugate and 5 μL of Annexin V-APC staining solution. Subsequently, the cells were incubated at room temperature for 30 min, then added 5 μL of PI, followed by further incubation at room temperature for 3 min, and added 300 μL of PBS, mixed well, then taken an ice bath, and finally tested on the machine immediately. The cells without any treatment were utilized as a control. Apoptotic changes were detected by flow cytometry.

Hemolysis Assay

Fresh blood, collected from the mice's eyeballs, was stabilized with an anticoagulant tube. The sample was centrifuged at 1500 rpm for 5 min, and washed six times with physiological saline until the supernatant was colorless, resulting in fresh red blood cells (RBCs). The erythrocytes were diluted in physiological saline to obtain a 2% erythrocyte suspension (RCS). After that, different concentrations of FEID were incubated with 2% RCS dispersion for 3 hours at 37°C. Meanwhile, equal volumes of ultrapure water and saline were selected as positive control (PC, 100% hemolysis) and negative control (NC, 0% hemolysis), respectively. All samples were centrifuged (4000 rpm, 5 min) and the supernatant was collected to monitor the hemoglobin content. Finally, the absorbance value of the supernatant was determined by UV-Vis spectrophotometer at 540 nm. The hemolysis rate was calculated as follows: hemolysis rate (%) = (sample-water) / (PBS- water) × 100%. Sample, PBS, and water are the absorbance values of the sample group, saline group, and ultrapure water group, respectively. The morphology of erythrocytes was visualized with a microscope.

Pharmacokinetics and BBB Permeability Analysis of FEID

For pharmacokinetic studies, blood circulation behavior of FEID in vivo was recorded. Mice were randomized into two groups (n = 3) and injected tail vein with FeCl$_3$ or FEID (Fe: 2 mg/kg, 200 μL). After mice were anesthetized with 10% chloralhydrate (30–40 μL/10g), blood samples (0.1 mL) were drawn from the retro-orbital sinus at 0, 2, 8, and 12 h after injection, and was deposited in an anticoagulation tube. Then all blood samples were digested by dropwise addition of 5 μL to 20 μL of a freshly prepared mixture of HNO$_3$ and H$_2$O$_2$ (4:1 volume ratio). After complete digestion, the Fe content of the supernatant was measured by ICP-MS.

To study the BBB permeability of FEID, the above batch of mice (two groups: one group (n = 3) was injected with PBS (200 μL, iv), the other group (n = 3) was treated with FEID (Fe: 2 mg/kg, 200 μL, iv)), 12 h after injection, were anesthetized with 10% chloralhydrate (30–40 μL/10g) and euthanized by cervical dislocation. The brains of mice from both groups were simultaneously extracted and stored in dry ice. 20–40 mg of the brain tissues from both groups were cut, and the individual pieces were weighed and placed in the bottom of a 10 mL centrifuge tube. Then the tissues were digested with HNO$_3$ and H$_2$O$_2$ in 4:1 vol % for 8h at 37 °C. After that, 1:1 vol % mixture of HNO$_3$ and H$_2$O$_2$ was added dropwise to the centrifuge tubes to digest the tissue overnight, then 0.3 mL of H$_2$O$_2$ was further added for final digestion. The element Fe was detected using ICP-MS.

Hematoxylin and Eosin (H&E) Staining

A new batch of mice were randomly divided into two groups (n=3), one group received FEID (Fe: 2 mg/kg, 200 μL, iv), and the control group received PBS (200 μL, iv). After 2 weeks, mice from both groups were anesthetized and euthanized through cervical dislocation, after which the main organs (heart, liver, spleen, lung, kidney) were collected. Organs were fixed in Paraformaldehyde solution (4%), followed by dehydration in graded ethanol, being embedded in paraffin and cut into 10 mm thick sections. Fixed sections were deparaffinized and hydrated according to a standard protocol and stained with H&E for microscopic observation.

Statistical Analysis

Data were expressed as mean ± standard deviation. Statistical analysis was conducted by t-test using GraphPad Prism 8, and significant difference was considered when $p < 0.05$.

Results and Discussions

Synthesis and Characterization of the FEID

Briefly, we integrated $FeCl_3$, ICG and DOX into a single nano system. Specially, the Fe^{3+}-ICG complex was formed through crosslinking between the anionic sulfonic acid group of ICG and Fe^{3+} ions. With the further help of iron ions, and electrostatic, π-π stacking, or hydrophobic interactions, the above three molecules were jointly assembled into uniform nanoplatform. To further explore the regular synthesis of FEID, we synthesized this nanoplatform by changing the synthetic method. From the TEM and DLS results, it was observed the distribution and size of the obtained nanoparticle were uneven when $FeCl_3$ and ICG were mixed for 3h. Followed by the addition of DOX (Figure S1), the size varied from a few nanometers to several hundred nanometers, which was unfavorable for subsequent biological applications. However, when $FeCl_3$, ICG and DOX aqueous solutions were mixed in the mass ratio of 1:1:1, the FEID exhibited a more uniform distribution, a regular and consistent spherical structure, and an average particle size of 78.2 nm in aqueous solution (Figure 1A and B). The formation of the stable structure should be attributed to the assistance of iron ions, which serves as a crucial factor in ensuring its suitability for further in vivo applications. We further explored the optimal synthesis time for FEID. It was shown that the absorption peaks of DOX and ICG were most pronounced after a synthesis time of 12 h, with no impurity peaks being observed (Figure 1C). Through analyzing the UV-vis-NIR spectra of ICG, DOX, $FeCl_3$ and FEID, both DOX and FEID exhibited significant absorption at 480 nm. And ICG alone demonstrated strong NIR absorption at 780 nm, whereas the absorption peak of FEID shifted to 808 nm. This shift in absorption peak confirmed the interaction between Fe^{3+} and ICG (Figure 1D). Furthermore, as shown in Figure S2A, when FEID was dispersed in phosphate buffer solution (PBS), fetal bovine serum (FBS), or DMEM for a duration of 3 days, its diameter exhibited negligible change (Figure S2C). And no distinct precipitation or PDI changes of FEID could be found in PBS and medium for 7 days (Figure S2D and E). This observation highlights the remarkable stability of FEID. The negatively charged surface of ICG, along with the presence of DOX and Fe ions, leads to an overall weak negative charge on the surface of the FEID (Figure S2B). XPS spectra further revealed the different signals of Fe (Figure 1E and F), providing evidence for the presence of Fe in FEID and confirming the successful formation of FEID. Additionally, by using ICP-MS, we confirmed that the content of Fe was detected at 0.9 Mm.
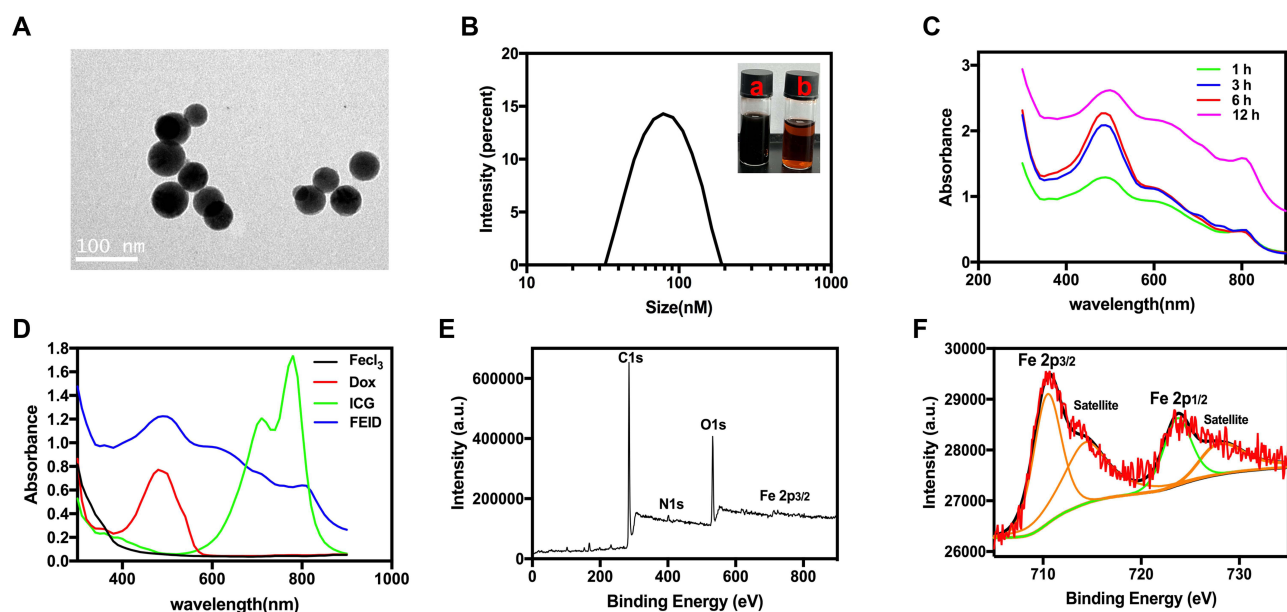

Figure 1 Synthesis and characterization of the FEID NPs. (**A**) TEM image of FEID. (**B**) Size distribution of FEID nanoplatform. The images of samples of FEID (a) and up solutions (b) are shown in the insets. (**C**) UV-Vis-NIR absorption spectra of FEID in the different times. (**D**) UV-Vis-NIR absorption spectra of $FeCl_3$, DOX, ICG and FEID. (**E**) XPS survey spectrum of FEID. (**F**) XPS spectra of the Fe 2p orbital for FEID.

Photothermal Properties of FEID

Given our intention to utilize the FEID in combination therapy for tumor treatment, we investigated whether the photothermal conversion capacity of ICG in the FEID was affected by other components. Here, a laser with a wavelength of 808 nm was employed to investigate the temperature changes after near-infrared radiation (Figure 2A). Under the irradiation of 1.0 W/cm², as shown in Figure 2B, the temperature of pure water (blank group) gradually rose from 24.8 °C to 37.5 °C, which was attributed to the photothermal effect resulting from the absorption of water. In contrast, the temperature change of the FEID exhibited a rapid increase from 26.1 °C at 0 s to 70.1 °C at 170 s, followed by a gradual stabilization at 73.1 °C. Furthermore, as depicted in Figure 2C, the photothermal effects of FEID were found to be independent of concentration and time. After 180 s of irradiation, concentrations above 12.5 μg/mL displayed no significant variation in the heating effect, which aligned with the highest fluorescence intensity observed at a concentration of 12.5 μg/mL. Our results suggest that the FEID can be a promising PTT agent for the treatment of cancer.

NIR Enhanced Fenton Reaction and Drug Release

As shown in Figure 3A, iron can act as a catalyst for the generation of hydroxyl radicals through Fenton-like reactions when combined with hydrogen peroxide. In this study, the changes in absorption of methylene blue (MB) and 3,3′,5,5′-tetramethylbenzidine (TMB) solutions were used to verify the capability of the FEID in generating •OH. To demonstrate the effect of pH on the Fenton reaction, FEID and H_2O_2 were treated together at different pH conditions, and the absorption intensity of the MB solution at 665 nm was significantly reduced (Figure 3B). In addition, the absorption
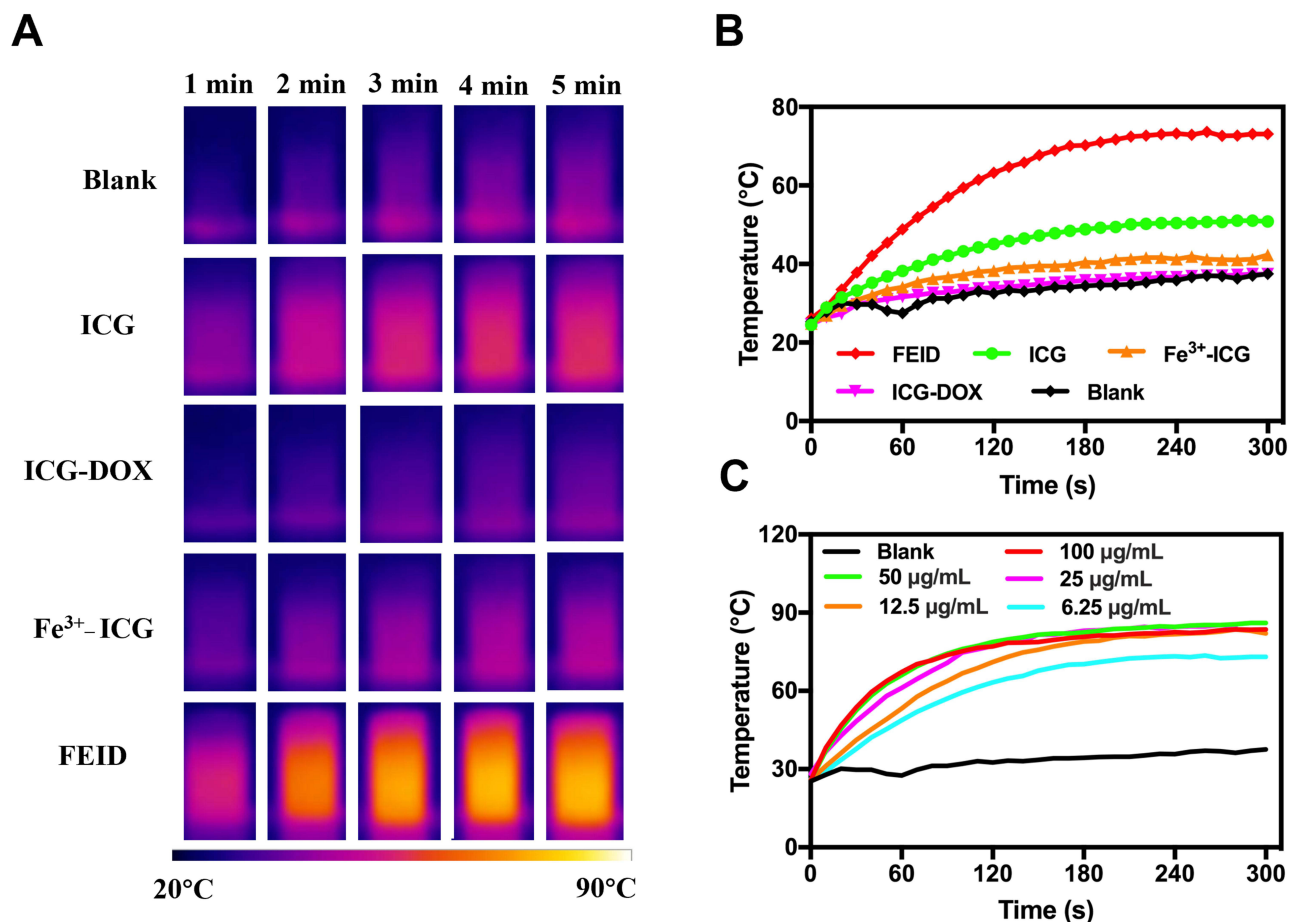

Figure 2 Photothermal properties of FEID NPs. (**A**) Infrared thermal images of FEID solutions irradiated with an 808 nm laser (1 W/cm²) from 0 to 5 min. (**B**) Photothermal curves of PBS, free ICG, Fe^{3+}-ICG, ICG-DOX and FEID solutions under the irradiation of an 808 nm laser with 1 W/cm² for 5 min. (**C**) Temperature changes of the FEID nanoplatform at different concentrations under 808 nm laser irradiation (1 W/cm², 5 min).
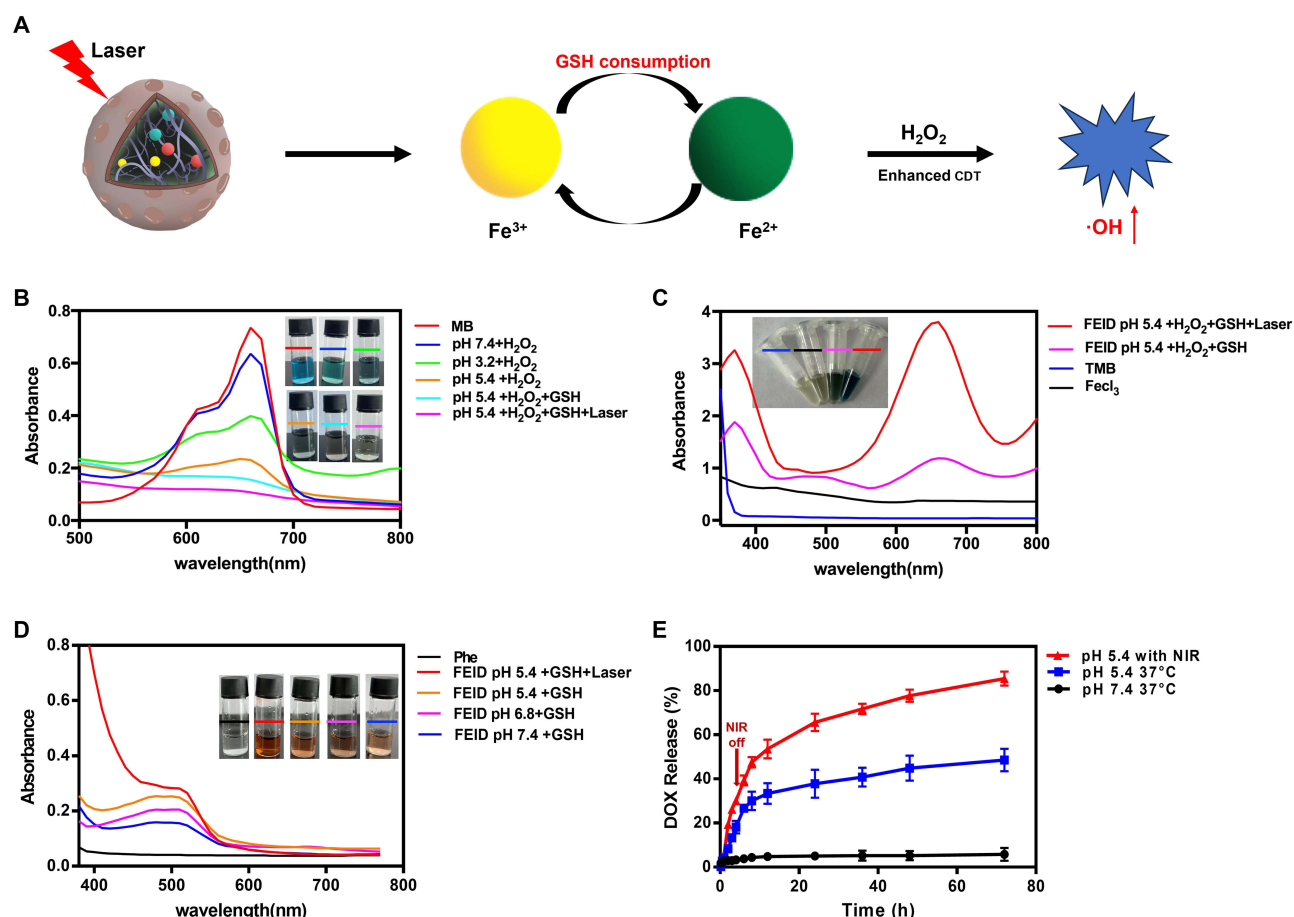
Figure 3 NIR enhanced Fenton reaction and drug release. (**A**) Schematic illustration of the capability of •OH generation and GSH depletion. (**B**) UV-Vis absorption spectra of MB treated with FEID in different groups. The inset in (**A**) are photographs of MB in different solutions. (**C**) UV-Vis absorption spectra of TMB after being treated with FEID. The inset shows photographs of TMB solutions in different solutions. (**D**) UV-Vis absorption spectra of the Phe and FEID/GSH/Phe with different groups, the inset shows their photographs. (**E**) The cumulative release of DOX from FEID under different pH values with or without Laser.

intensity demonstrated a correlation with pH, with the FEID exhibiting the highest ability to generate •OH at a pH of 5.4, which overcame the pH limitation (pH 2–4) typically associated with the CDT effect of traditional Fenton reagents. Similarly, the TMB solution treated with a mixture of H_2O_2 and FEID at pH 5.4 showed a significant absorption peak at 665 nm in the UV-vis spectrum, which also confirmed the ability of producing •OH of FEID (Figure 3C). Our findings indicate that the FEID possesses CDT efficiency in tumor treatment.

Considering that temperature changes could cause an acceleration of the Fenton reaction, we further investigated the photothermal enhancement of CDT performance of FEID. As shown in Figure 3B and C, the FEID nanoplatform first underwent a reaction with H_2O_2 at pH 5.4 and then were irradiated with an 808 nm laser for 5 min, resulting in a noticeable decrease in MB absorbance and an increase in TMB absorbance. This observation provided clear evidence that the temperature rise induced by FEID accelerated the Fenton reaction. Our results demonstrate that the FEID could achieve CDT/PTT synergistic therapy.

Moreover, GSH consumption plays a key role in enhancing CDT. To investigate the ability of FEID in consuming GSH in acidic environments, we utilized the 1,10-phenanthroline (Phe) indicator, which is widely known to react with Fe^{2+} to form an orange-red complex with maximum absorption at 510 nm, indicating a change in the concentration of divalent iron ions. As shown in Figure 3D, the consumption of GSH in the Fenton reaction mediated by FEID was pH dependent. Compared to neutral environments, the accelerated dissociation of FEID in acidic environments, coupled with laser irradiation, led to a higher consumption of GSH at pH 5.4. These results suggest the potential application of the FEID in down-regulating GSH in tumors, thus enabling GSH-deprived CDT enhancement for tumor therapy.

Next, we used DOX as a model to study pH/photothermal enhanced drug release behavior. By establishing a linear relationship between absorbance and DOX concentration, the encapsulation efficiency of DOX was determined to be 53.1%, while the loading content was found to be 17.7%. The high loading efficiency could be attributed to the carrier-free drug-loaded system and the electrostatic absorption between the positively charged DOX and the negatively charged ICG. To simulate the acidic environment of lysosomes in vitro, DOX release experiments were conducted in PBS buffer (pH=5.4) and compared with that in pH=7.4. In Figure 3E, it can be observed that in PBS (pH=7.4, 37°C), only 5.83% of DOX was released at 72 h, showing a slow-release behavior. However, in an acidic buffer (pH=5.4, 37°C), the release of DOX increased to 40.52%, which was significantly higher than that in PBS. This phenomenon indicated that FEID was pH responsive and may become more porous in acidic environments, facilitating the release of DOX. Given the thermal response capability of FEID and the significant warming effect of FEID under laser irradiation, we further investigated the NIR-promoted drug release properties of FEID in PBS (pH=5.4) and monitored the release process after irradiation at 808 nm. The results revealed that the release of DOX increased to 85.42% within 72 h (Figure 3E), indicating that FEID could rapidly release chemotherapy drugs upon laser irradiation. This effect was attributed to FEID's ability to respond to acidity and undergo sharp disintegration due to local heating.[41–43] Additionally, the size and distribution of FEID were significantly altered under 1 W/cm^2 laser irradiation, with the size reducing to 28.20 nm after 5 min of irradiation (Figure S2F). Overall, these findings suggest that temperature changes can accelerate drug release from the FEID under relatively low pH conditions.

NIR Triggered Fluorescence Imaging and Magnetic Resonance Imaging

Image-guided therapy plays a crucial role in determining the optimal treatment window. To investigate the effects of the FEID on near-infrared fluorescence imaging and MR imaging, we utilized ICG as a fluorescent dye, which had an excitation wavelength of 780 nm and an emission wavelength of 810 nm. By measuring the fluorescence of FEID, we could examine the interactions between metals and drugs. As depicted in Figure 4A and C, the combination of ICG with Fe^{3+} and DOX resulted in significant fluorescence quenching. This is mainly attributed to the strong and complex interactions between the ICG, DOX, and Fe^{3+}, which play an important role in maintaining the stability of FEID in blood circulation. Subsequently, we assessed the fluorescence imaging performance of the FEID following laser irradiation. It was observed that after 808 nm laser irradiation, the FEID were activated by light, leading to the restoration of their fluorescence (Figure 4B and D), suggesting the collapse of the FEID, the subsequent release of ICG upon laser irradiation, and the released ICG transferred from a closed state, where aggression caused quenching, to a state of fluorescence recovery, enabling fluorescence imaging of tumor tissue. This process achieves controllable activation of ICG fluorescence, the dynamic changes in ICG fluorescence are different from other static imaging techniques such as CT/MRI or non-specific dye staining, allowing for real-time display of tumor boundaries. Additionally, the fluorescent signals of DOX also demonstrated that the heat generated by FEID effectively triggered the release of DOX. This light-responsive property enabled targeted drug release at the tumor site, thereby improving treatment efficiency and minimizing side effects. The poor stability of dye in solutions and the complex relationship between their fluorescence intensity and dye concentration pose great challenges for clinical applications. Typically, higher dye concentrations result in stronger fluorescence, but this is not the case for ICG fluorescence.

ICG fluorescence is influenced by factors such as the formation of aggregates at high concentrations, concentration quenching (ie, self-quenching), and overlapping dye absorption and emission spectra. In this study, we found the fluorescence intensity of the FEID solution peaked at an ICG concentration of 12.5 ug/mL (Figure 4E) when being irradiated with a laser. Beyond this concentration, the fluorescence intensity would decrease. This finding is important for determining the optimal concentration of FEID to achieve maximum effect in the body, which could avoid side effects suffering from unnecessary additional doses.

Tumor magnetic resonance imaging is of great significance for tumor surveillance, efficacy evaluation and surgical navigation, which is achieved by using contrast agents. And iron nanoparticles have shown promise as reagents for T2-weighted MRI. In our study, we evaluated the in vitro MR imaging capability of FEID and obtained T2-weighted MR images at various concentrations (Figure 4F). These results exhibited that the signal intensity of T2-weighted imaging
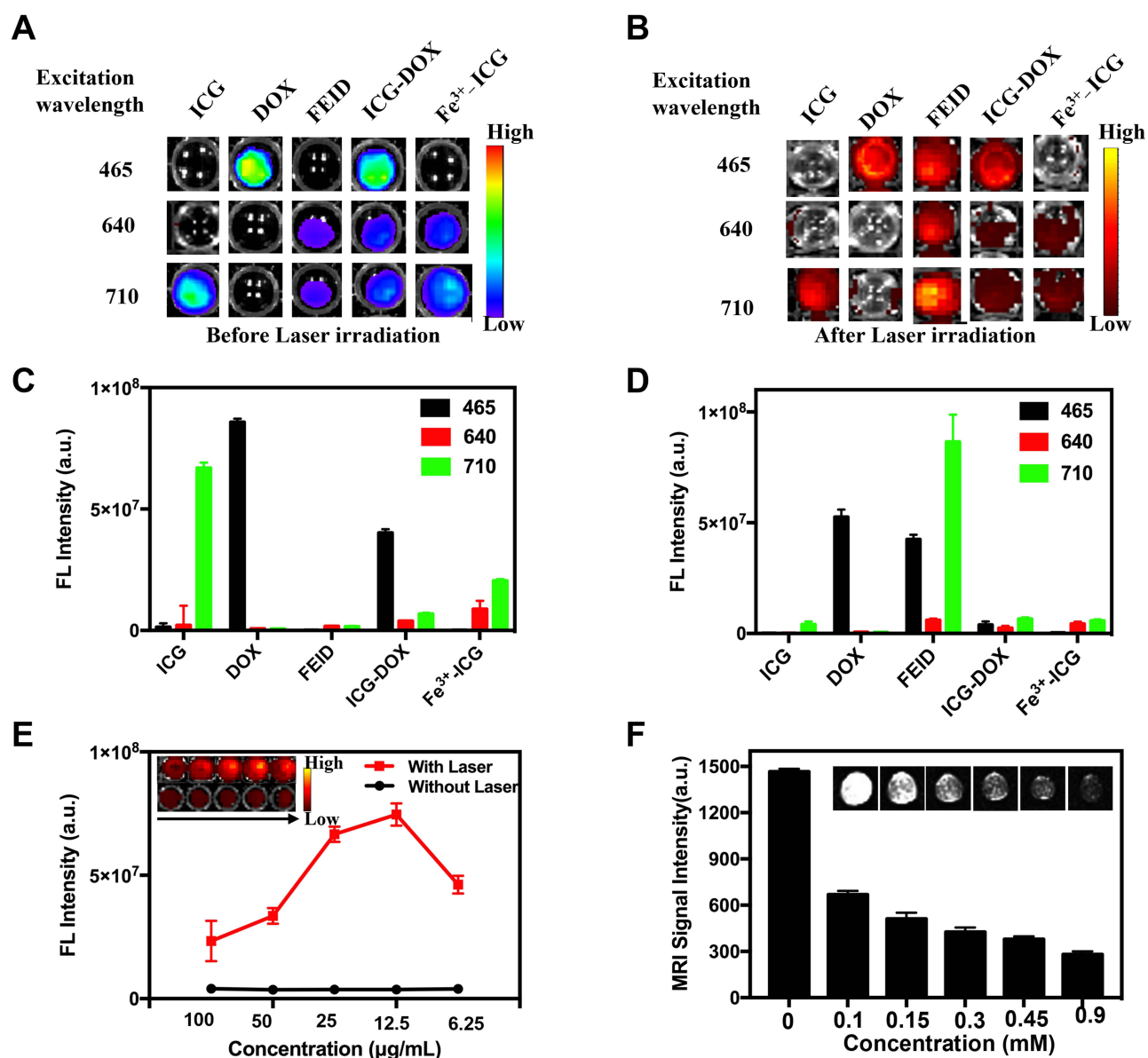
Figure 4 NIR triggered fluorescence imaging and magnetic resonance imaging. (**A**) Fluorescence quenching of ICG and DOX, indicating the complex interactions among the Fe^{3+}, ICG and DOX (ICG concentration: 12.5 μg/mL). (**B**) Fluorescence recovery of ICG and DOX after laser irradiation ($1W/cm^2$, 5 min, ICG concentration: 12.5 μg/mL). (**C**) and (**D**) Fluorescence signal intensity of different groups before and after laser irradiation. (**E**) Fluorescence changes of FEID at various concentrations of ICG before or after irradiation ($1W/cm^2$, 5 min). (**F**) MRI values of various concentrations of FEID in vitro. Inset: the MRI images of FEID at different concentrations.

exhibited a positive correlation with concentration of FEID. Collectively, our findings demonstrate the ability of FEID for NIR triggered fluorescence imaging and magnetic resonance imaging.

Evaluation of Cellular Uptake and ROS Generation

To investigate the subcellular localization of FEID in U87MG cells before and after near-infrared light stimulation, we further utilized confocal laser scanning microscopy (CLSM), flow cytometry and inverted fluorescence microscopy to examine the cellular uptake and drug distribution. As shown in Figure 5A and S3, the red fluorescence signal of DOX alone was primarily observed in the cytoplasm. However, when U87MG cells were treated with FEID, the red fluorescent signal was detected in the cytoplasm, indicating that FEID was efficiently taken up by the tumor cells. Furthermore, DOX distribution was detected in the nucleus, suggesting that FEID-treated cells could be retained in the tumor cells and slowly released into the nucleus, leading to cell death. Notably, U87MG cells incubated with FEID and then exposed to
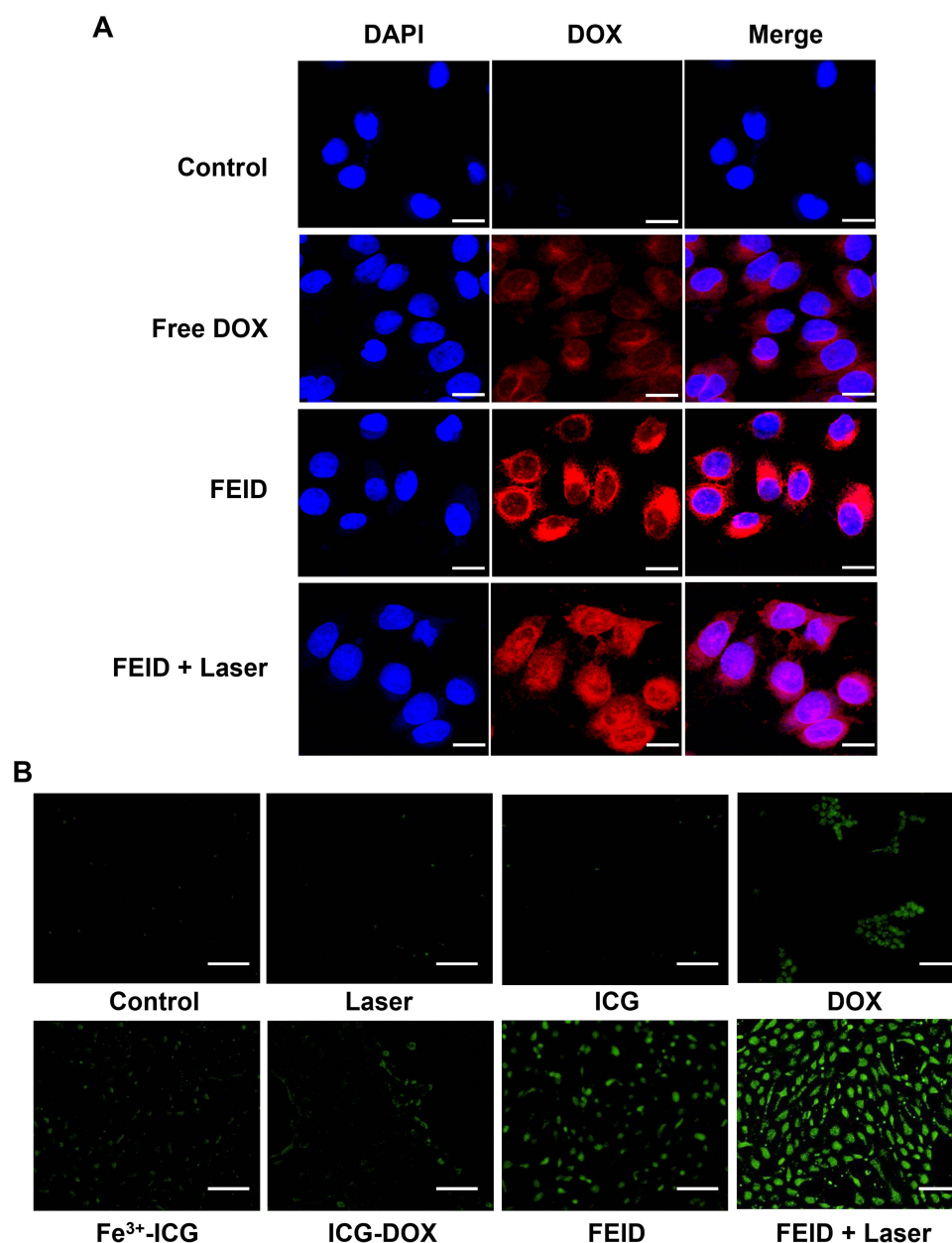
Figure 5 Evaluation of cellular uptake and ROS generation. (**A**) Cellular uptake of the FEID in U87MG cells. (Scale bar: 50 μm). (**B**) Fluorescence microscope images of ROS generation in U87MG cells that received different treatments ([Fe]: 0.9mM, Scale bar: 200 μm).

laser exhibited a distinct red fluorescence signal in the nucleus. This observation suggested that heating induced by the laser promoted the release of DOX from FEID, resulting in a significant accumulation of DOX in the nucleus. The quantification of DOX inside the nucleus was performed using image J software (Figure S4). The flow cytometric results also exhibited a substantial fluorescence intensity enhancement at the prolonged duration of incubation (Figure S5). These findings confirm that photothermal effects mediated by FEID could enhance the accumulation of chemotherapy drugs in tumor cells, thereby facilitating the efficacy of chemotherapy.

Next, we further utilize 2′,7′-dichlorodihydrofluorescein diacetate (DCFH-DA) to estimate intracellular ROS levels. DCFH-DA is oxidized to 2′,7′-dichlorofluorescein by intracellular ROS, emitting bright green fluorescence. As shown in Figure 5B, minimal fluorescence was observed in the control, ICG, Fe^{3+}-ICG, and laser irradiation groups, indicating low intracellular ROS levels. However, the fluorescence intensity of the DOX group and the ICG-DOX group was slightly higher than that of the PBS group, as DOX induced an increase in intracellular H_2O_2 levels. After co-incubation with

FEID, a green, fluorescent signal was also detected since FEID underwent a Fenton reaction with endogenous H_2O_2 in tumor cells, producing •OH. Notably, U87MG cells treated with FEID after being irradiated for 5 min exhibited the brightest green fluorescence, which was attributed to that the increase in temperature induced by FEID accelerated the Fenton reaction and enhanced the release of DOX. Collectively, our results suggest that FEID can effectively induce the production of intracellular ROS, leading to apoptosis.

CDT Enhanced Cytotoxicity Assay of FEID

FEID, in combination with the tumor microenvironment and near-infrared light response, showed a promising potential for treating cancer cells through synergistic effects. However, its cytotoxicity remained unclear. We thus performed MTT assay by using 293T and immune cells: RAW264.7. After a 24h incubation with DOX concentrations ranging from 0 to 15 μg/mL, the survival rate of 293T cells and RAW264.7 cells remained above 90%, indicating that FEID was highly biocompatible with normal cells (Figure 6A).
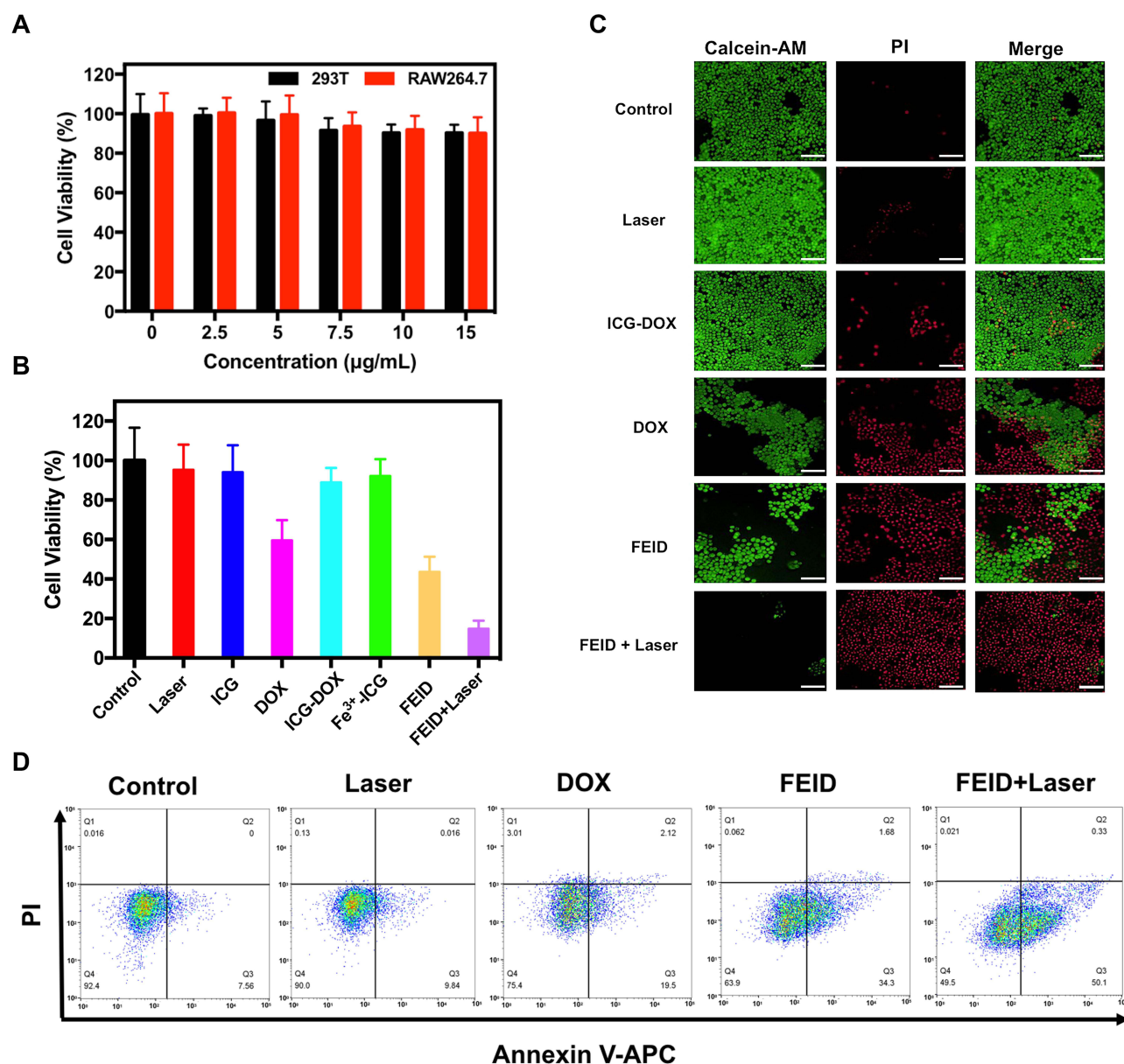

Figure 6 In vitro cytotoxicity profiles of the FEID NPs. (**A**) MTT assay of 293T cells treated with the FEID for 24 h. (**B**) U87MG cells viability after treatment with various groups with or without 808 nm laser irradiation (1 W/cm^2) for 5 min. (**C**) Live/dead cell staining results of U87MG cells co-stained with Calcein-AM (live cells, green) and PI (dead cells, red) after different treatments (Scale bar: 200 μm). (**D**) Apoptosis evaluation of U87MG cells after different treatments.

Subsequently, the cytotoxicity of FEID in combination with laser irradiation was further evaluated on U87MG cells. As shown in Figure 6B, it could be observed that there was no significant cytotoxicity on U87MG cells treated in the control, free ICG, only laser irradiation, and Fe^{3+}-ICG groups when exposed to the same amount of doxorubicin. However, the co-incubation of U87MG cells with FEID resulted in a significant inhibition of cell proliferation, with an inhibition rate of 56.37% in the ICG-DOX group. Moreover, when the FEID-incubated tumor cells were exposed to 808 nm laser irradiation, the inhibition rate increased to 85.21%. Our results suggested that the combination of CDT, PTT and chemotherapy could significantly enhance the anti-tumor effect.

The cytotoxicity of FEID to U87MG cells was further confirmed by using the live/dead cell staining assay. No obvious red fluorescence signal was observed in the control, laser irradiation, and ICG groups, indicating no significant cytotoxicity to tumor cells from ICG alone or irradiation (Figure 6C). However, in the FEID group, distinct red fluorescence was observed compared to the control group, showing the cytotoxicity of the FEID to tumor cells. Furthermore, U87MG cells incubated with FEID and co-treated with 808 nm laser irradiation showed the strongest red fluorescence, indicating that FEID in combination with laser treatment had a potent effect in eliminating tumor cells.

For the further evaluation of apoptosis levels, the U87MG cells with different treatments were analyzed by flow cytometry after dying with Annexin V-APC and PI. The apoptosis rates of FEID-treated cells were much higher than that of laser only and free DOX-treated cells. Notably, the FEID with laser-treated cells had the highest apoptosis ratio of 50.43% (Figure 6D and S6). These findings suggested that the superior antitumor activity of FEID could be attributed to the synergistic effects of FEID with CDT/PTT/chemotherapy combination therapy. Overall, these results highlight the potential of FEID as a promising therapeutic agent for cancer treatment.

Biocompatibility, Pharmacokinetics, and BBB Permeability Analysis of FEID

To determine the biosafety of the FEID on blood cells, we conducted an incubation experiment using different concentrations of FEID with erythrocytes of mice. As shown in Figure 7A, the rate of hemolysis was found to be lower than the internationally accepted standard of 5%. Furthermore, the integrity of the erythrocytes was confirmed
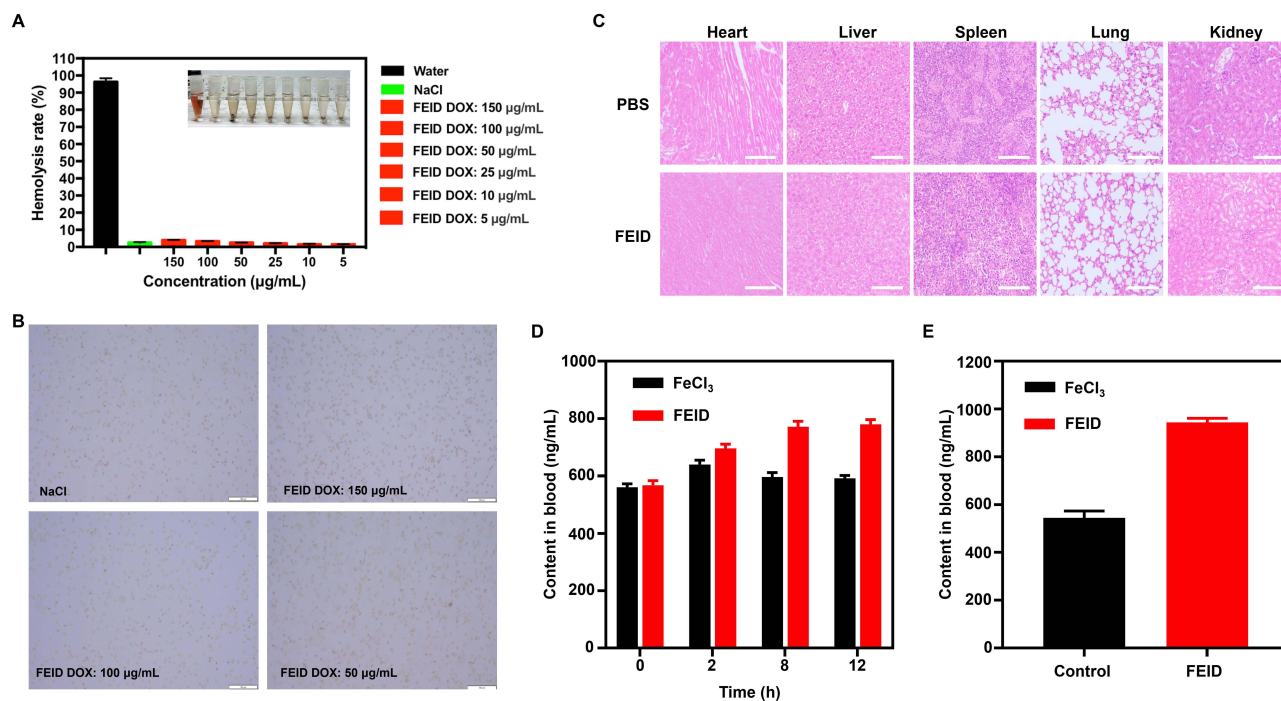

Figure 7 Safety assessment and distribution of FEID NPs. (**A**) In vitro hemolysis percentage of FEID incubated with rabbit red blood cells. The inset image showed RBCs treated with FEID at various concentrations. (**B**) Representative photos of the integrity of erythrocytes (Scale bar: 100 μm). (**C**) H&E staining of tissues from major organs of mice after various treatment (Scale bar: 200 μm). (**D**) The in vivo biodistribution analysis using ICP-MS for blood of the $FeCl_3$ and FEID injected mice as a function of time. (**E**) The content of the Fe in the brain of the $FeCl_3$ and FEID injected mice.

through microscopy observation (Figure 7B), showing that all concentrations of FEID exhibited non-hemolytic behavior after incubation with erythrocytes.

Besides, free DOX causes early signs of toxic cardiomyopathy, which is characterized by cardiac muscle cell striation disruption and granularity with some eosinophilic and vacuolated sarcoplasm and pyknotic endothelial cell nuclei in the capillary network.[44] To evaluate the safety of drug delivery systems, we randomly divided the mice into two groups. One group was injected with FEID, and the control group was injected with PBS. After 2 weeks, the main organs were collected. And no significant damage was found in the heart, liver, spleen, lung, and kidney of mice treated with FEID compared to that from PBS group (Figure 7C), demonstrating that the self-assembly of FEID reduced the toxicity of DOX in vivo.

Long blood circulation is a prerequisite for designing a desirable drug delivery system. The design and development of carriers with tunable structural and physical properties have achieved the goal of improving blood circulation. Gu et al constructed a two-dimensional ultrathin layered hydroxide (LDH) nanosheet with high drug loading, good colloidal stability, and extended blood circulation for cancer therapy. The pH-sensitive drug release behavior facilitated the mitigation of premature drug release in the blood circulation, achieved tumor-selective release of DOX, enhanced anticancer efficacy, and reduced the toxicity of DOX to normal tissues.[45]

To investigate the blood circulation time of FEID, we measured the plasma concentration of Fe by using ICP-MS over time after intravenous injection of $FeCl_3$ and FEID in mice. As shown in Figure 7D, after intravenous administration, free Fe was quickly excreted from the circulatory system. In contrast, the circulation time of FEID showed much longer than the group treated with free $FeCl_3$ over time, indicating that nano materialization prolonged the circulation and retention time of the drug in the blood.

The physical barrier caused by BBB is widely recognized as the key hinder for satisfactory drug treatment for glioblastoma. With the development of nanotechnology, more and more studies have proved that the FEID have the advantage of permeating the blood-brain barrier.[44,46] By using ICP-MS, our results indicated the good BBB permeability ability of FEID in mice (Figure 7E). Moreover, FEID had a longer retention time compared to control group, suggesting its promising potential as a superior anti-tumor drug.

Conclusion

In summary, a novel anti-tumor FEID nanoplatform was developed using a simple self-assembly method for the CDT/PTT/chemotherapy combination tumor therapy. Under weak acidity and laser irradiation conditions, the prepared FEID was able to release substances such as Fe^{3+}, ICG and DOX. The released Fe^{3+} acted as a Fenton-like agent for CDT. In addition, the highly expressed GSH in the tumor cells reduced Fe^{3+} to Fe^{2+}, which further catalyzed H_2O_2 to produce toxic •OH. Meanwhile, the deprivation of GSH also enhanced CDT. Moreover, FEID exhibits remarkable photothermal effects for PTT, improving the efficiency of CDT and promoting the release of DOX. More importantly, FEID showed the fluorescence recovery effect upon near-infrared light stimulation, enabling precise tumor diagnosis. In vitro experimental results confirmed the superior anti-tumor effect of FEID. Their low toxicity and blood-brain barrier permeability demonstrate their anti-tumor potential in vivo. Subsequent work should focus on animal models of glioblastoma to evaluate the systemic clearance, biodistribution, long-term biocompatibility toxicity and combination therapy effect of FEID. Overall, this nanoplatform holds great promise as an integrated approach for the diagnosis and treatment of glioblastoma with CDT/PTT/chemotherapy.

Author Contributions

All authors made a significant contribution to the work reported, whether that is in the conception, study design, execution, acquisition of data, analysis and interpretation, or in all these areas; took part in drafting, revising or critically reviewing the article; gave final approval of the version to be published; have agreed on the journal to which the article has been submitted; and agreed to be accountable for all aspects of the work.

Funding

Disclosure

The authors report that there are no conflicts of interest in this work.

References

1. Ostrom QT, Price M, Neff C, et al. CBTRUS Statistical Report: primary Brain and Other Central Nervous System Tumors Diagnosed in the United States in 2015–2019. *Neuro Oncol.* 2022;25(Supplement_4):iv1–iv99. doi:10.1093/neuonc/noad149

2. Omuro A, Brandes AA, Carpentier AF, et al. Radiotherapy combined with nivolumab or temozolomide for newly diagnosed glioblastoma with unmethylated MGMT promoter: an international randomized Phase III trial. *Neuro Oncol.* 2023;25(1):123–134. doi:10.1093/neuonc/noac099

3. Jiang N, Xie B, Xiao W, et al. Fatty acid oxidation fuels glioblastoma radioresistance with CD47-mediated immune evasion. *Nat Commun.* 2022;13(1):1511. doi:10.1038/s41467-022-29137-3

4. Yu H, Teng Y, Ge J, et al. Isoginkgetin-loaded reactive oxygen species scavenging nanoparticles ameliorate intervertebral disc degeneration via enhancing autophagy in nucleus pulposus cells. *J Nanobiotechnology.* 2023;21(1):99. doi:10.1186/s12951-023-01856-9

5. Huang L, Zhu J, Xiong W, et al. Tumor-Generated Reactive Oxygen Species Storm for High-Performance Ferroptosis Therapy. *ACS Nano.* 2023;17(12):11492–11506. doi:10.1021/acsnano.3c01369

6. Zhao S, Lai K, Gao Z, et al. Reactive oxygen species nanoamplifiers with multi-enzymatic activities for enhanced tumor therapy. *Nanoscale.* 2023;15(22):9652–9662. doi:10.1039/d3nr00107e

7. Yang B, Chen Y, Shi J. Reactive Oxygen Species (ROS)-Based Nanomedicine. *Chem Rev.* 2019;119(8):4881–4985. doi:10.1021/acs.chemrev.8b00626

8. Dirersa WB, Kan TC, Getachew G, et al. Preclinical Assessment of Enhanced Chemodynamic Therapy by an FeMnOx-Based Nanocarrier: tumor-Microenvironment-Mediated Fenton Reaction and ROS-Induced Chemotherapeutic for Boosted Antitumor Activity. *ACS Appl Mater Interfaces.* 2023;15(48):55258–55275. doi:10.1021/acsami.3c10733

9. Dirersa WB, Kan TC, Chang JS, et al. Engineering H_2O_2 Self-Supplying Platform for Xdynamic Therapies via Ru–Cu Peroxide Nanocarrier: tumor Microenvironment-Mediated Synergistic Therapy. *ACS Appl Mater Interfaces.* 2024;16(19):24172–24190. doi:10.1021/acsami.3c18888

10. Ma ZL, Bai RN, Yu W, et al. Copper-cobalt diatomic bifunctional oxygen electrocatalysts based on three-dimensional porous nitrogen-doped carbon frameworks for high-performance zinc-air batteries. *J Colloid Interface Sci.* 2025;683:1150–1161. doi:10.1016/j.jcis.2024.12.139

11. Sun Y, Sun X, Li X, et al. A versatile nanocomposite based on nanoceria for antibacterial enhancement and protection from aPDT-aggravated inflammation via modulation of macrophage polarization. *Biomaterials.* 2021;268:120614. doi:10.1016/j.biomaterials.2020.120614

12. Wu P, Dong W, Guo X, et al. ROS-Responsive Blended Nanoparticles: cascade-Amplifying Synergistic Effects of Sonochemotherapy with On-demand Boosted Drug Release During SDT Process. *Adv Healthc Mater.* 2023;12(2):e2203109. doi:10.1002/adhm.201900720

13. Zhang WQ, Hu ZH, Tian J, et al. A narrative review of near-infrared fluorescence imaging in hepatectomy for hepatocellular carcinoma. *Ann Transl Med.* 2021;9(2):171. doi:10.21037/atm-20-5341

14. Yang J, Ma S, Xu R, et al. Smart biomimetic metal organic frameworks based on ROS-ferroptosis-glycolysis regulation for enhanced tumor chemo-immunotherapy. *J Control Release.* 2021;334:21–33. doi:10.1016/j.jconrel.2021.04.013

15. Zhang C, Bu W, Ni D, et al. Synthesis of Iron Nanometallic Glasses and Their Application in Cancer Therapy by a Localized Fenton Reaction. *Angew Chem Int Ed Engl.* 2016;55(6):2101–2106. doi:10.1002/anie.201510031

16. Tan J, Duan X, Zhang F, et al. Theranostic Nanomedicine for Synergistic Chemodynamic Therapy and Chemotherapy of Orthotopic Glioma. *Adv Sci.* 2020;7(24):2003036. doi:10.1002/advs.202003036

17. Wang S, Yu G, Yang W, et al. Photodynamic-Chemodynamic Cascade Reactions for Efficient Drug Delivery and Enhanced Combination Therapy. *Adv Sci.* 2021;8(10):2002927. doi:10.1002/advs.202002927

18. Li C, Wan Y, Zhang Y, et al. In Situ Sprayed Starvation/Chemodynamic Therapeutic Gel for Post-Surgical Treatment of IDH1 (R132H) Glioma. *Adv Mater.* 2022;34(5):e2103980. doi:10.1002/adma.202103980

19. Yang J, Dai D, Zhang X, et al. Multifunctional metal-organic framework (MOF)-based nanoplatforms for cancer therapy: from single to combination therapy. *Theranostics.* 2023;13(1):295–323. doi:10.7150/thno.80687

20. Yue Y, Zhao X. Melanin-Like Nanomedicine in Photothermal Therapy Applications. *Int J Mol Sci.* 2021;22(1):399. doi:10.3390/ijms22010399

21. Zhi D, Yang T, O'Hagan J, et al. Photothermal therapy. *J Control Release.* 2020;325:52–71. doi:10.1016/j.jconrel.2020.06.032

22. Ma X, Chen B, Wu H, et al. A tumour microenvironment-mediated $Bi_{2-x}Mn_xO_3$ hollow nanospheres via glutathione depletion for photothermal enhanced chemodynamic collaborative therapy. *J Mater Chem B.* 2020;10(18):3452–3461. doi:10.1039/d2tb00398h

23. Li Y, Ding Y, Zhang Y, et al. An engineered cascade-sensitized red-emitting upconversion nanoplatform with a tandem hydrophobic hydration-shell and metal-phenolic network decoration for single 808 nm triggered simultaneous tumor PDT and PTT enhanced CDT. *Nanoscale.* 2023;15(23):10067–10078. doi:10.1039/d2nr06776e

24. Wang S, Wang Z, Yu G, et al. Tumor-Specific Drug Release and Reactive Oxygen Species Generation for Cancer Chemo/Chemodynamic Combination Therapy. *Adv Sci.* 2019;6(5):1801986. doi:10.1002/advs.201801986

25. Huang Y, Guan Z, Ren L, et al. Bortezomib prodrug catalytic nanoreactor for chemo/chemodynamic therapy and macrophage re-education. *J Control Release.* 2022;350:332–349. doi:10.1016/j.jconrel.2022.08.037

26. Du C, Wang C, Jiang S, et al. pH/GSH dual-responsive supramolecular nanomedicine for hypoxia-activated combination therapy. *Biomater Sci.* 2023;11(16):5674–5679. doi:10.1039/d3bm00519d

27. Wang Y, Xie L, Li X, et al. Chemo-immunotherapy by dual-enzyme responsive peptide self-assembling abolish melanoma. *Bioact Mater.* 2023;16:549–562. doi:10.1016/j.bioactmat.2023.09.006

28. Liu H, Deng Z, Li T, et al. Fabrication, GSH-responsive drug release, and anticancer properties of thioctic acid-based intelligent hydrogels. *Colloids Surf B Biointerfaces.* 2022;217:112703. doi:10.1016/j.colsurfb.2022.112703

29. Chen Q, Li X, Xie Y, et al. Azo modified hyaluronic acid based nanocapsules: CD44 targeted, UV-responsive decomposition and drug release in liver cancer cells. *Carbohydr Polym.* 2021;267:118152. doi:10.1016/j.carbpol.2021.118152

30. Getachew G, Hsiao C-H, Wibrianto A, et al. High performance carbon dots based prodrug Platform: image-Guided photodynamic and chemotherapy with On-Demand drug release upon laser irradiation. *J Colloid Interface Sci.* 2023;633:396–410. doi:10.1016/j.jcis.2022.11.112

31. Wang J, Zhou Q, Dong Q, et al. Nanoarchitectonic Engineering of Thermal-Responsive Magnetic Nanorobot Collectives for Intracranial Aneurysm Therapy. *Small*. 2024;20:e2400408. doi:10.1002/smll.202400408

32. Jia L, Li X, Liu H, et al. Ultrasound-enhanced precision tumor theranostics using cell membrane-coated and pH-responsive nanoclusters assembled from ultrasmall iron oxide nanoparticles. *Nano Today*. 2021;36:101022. doi:10.1016/j.nantod.2020.101022

33. Chawla S, Bukhari S, Afridi OM, et al. Metabolic and physiologic magnetic resonance imaging in distinguishing true progression from pseudoprogression in patients with glioblastoma. *NMR Biomed*. 2022;35(7):e4719. doi:10.1002/nbm.4719

34. Zhang Z, Lu M, Chen C, et al. Holo-lactoferrin: the link between ferroptosis and radiotherapy in triple-negative breast cancer. *Theranostics*. 2021;11(7):3167–3182. doi:10.7150/thno.52028

35. Wang X, Hu Y, Wu X, et al. Near-infrared fluorescence imaging-guided lymphatic mapping in thoracic esophageal cancer surgery. *Surg Endosc*. 2022;36(6):3994–4003. doi:10.1007/s00464-021-08720-7

36. Wakabayashi T, Cacciaguerra AB, Abe Y, et al. Indocyanine Green Fluorescence Navigation in Liver Surgery: a Systematic Review on Dose and Timing of Administration. *Ann Surg*. 2022;275(6):1025–1034. doi:10.1097/SLA.0000000000005406

37. Egloff-Juras C, Bezdetnaya L, Dolivet G, et al. NIR fluorescence-guided tumor surgery: new strategies for the use of indocyanine green. *Int J Nanomed*. 2019;25:7823–7838. doi:10.2147/IJN.S207486

38. Wu X, Wang R, Kwon N, et al. Activatable fluorescent probes for in situ imaging of enzymes. *Chem Soc Rev*. 2022;51(2):450–463. doi:10.1039/d1cs00543j

39. Zhang X, Li S, Ma H, et al. Activatable NIR-II organic fluorescent probes for bioimaging. *Theranostics*. 2022;12(7):3345–3371. doi:10.7150/thno.71359

40. Miao J, Miao M, Jiang Y, et al. An Activatable NIR-II Fluorescent Reporter for In Vivo Imaging of Amyloid-β Plaques. *Angew Chem Int Ed Engl*. 2023;62(7):e202216351. doi:10.1002/anie.202216351

41. Liu J, Bu W, Pan L, et al. NIR-triggered anticancer drug delivery by upconverting nanoparticles with integrated azobenzene-modified mesoporous silica. *Angew Chem Int Ed*. 2013;52(16):4375–4379. doi:10.1002/anie.201300183

42. Zhong Y, Wang C, Cheng L, et al. Gold nanorod-cored biodegradable micelles as a robust and remotely controllable doxorubicin release system for potent inhibition of drug-sensitive and resistant cancer cells. *Biomacromolecules*. 2013;14(7):2411–2419. doi:10.1021/bm400530d

43. Cai X, Zeng Z, Hong L, et al. The role of toll-like receptors in myocardial toxicity induced by doxorubicin. *Immunol Lett*. 2020;217:56–64. doi:10.1016/j.imlet.2019.11.001

44. Li J, Zhao J, Tan T, et al. Nanoparticle Drug Delivery System for Glioma and Its Efficacy Improvement Strategies: a Comprehensive Review. *Int J Nanomed*. 2020;15:2563–2582. doi:10.2147/IJN.S243223

45. Zhang H, Zhang L, Cao Z, et al. Two-dimensional ultra-thin nanosheets with extraordinarily high drug loading and long blood circulation for cancer therapy. *Small*. 2022;18(22):e2200299. doi:10.1002/smll.202200299

46. Li W, Qiu J, Li X, et al. BBB pathophysiology–independent delivery of siRNA in traumatic brain injury. *Sci Adv*. 2021;7(1):eabd6889. doi:10.1126/sciadv.abd6889